6.4 Strain Analysis

6.4.1 Introduction

Soil strains associated with pile movements during both impact installation and static-loading have been estimated from the grain displacement contour diagrams using the finite element solids of revolution idealisation described in Appendix D. All the stain diagrams referred to in this section, which includes Figures 6.7 to 6.44, can be found in the rear pocket of this volume. The 222 element rectangular grid shown in Figure 6.7 was used to convert the impact installation grain displacement data to major and minor principal strains, principal strain directions, maximum shear strains and volumetric strains occurring on a radial plane. Circumferential strains have also been plotted. Horizontal and vertical displacement components were extrapolated from the displacement contour diagrams to the nodes of the grid in Figure 6.7, and the strain contour diagrams of Figures 6.8 to 6.19 were drawn from the calculated strains. Similar data was generated from the grain displacement diagrams showing soil movements measured during static load testing using the 290 element rectangular grid shown in Figure 6.20. The corresponding strain contour diagrams are given in Figures 6.21 to 6.44. Some of the strain diagrams have been partially coloured to clarify complex strain patterns.

The sign notation used for the strain contour diagram corresponds to that given by Atkinson and Bransby (1978). Thus, major and minor principal strains and circumferential strains are shown as positive when compressive. Volumetric strains are accordingly shown as positive when volume decrease occurred. Postive shear strains indicate that counter-clockwise rotation of an element boundary occurred. Further, the shear strains given refer to pure shear strain rather than "engineers" or simple shear strain. The magnitude of pure shear strain is half that of simple shear strain which includes a component of rigid body rotation. (See Atkinson and Bransby [1978], page 16 and pages 38 to 39.)

The contours in the shear strain diagrams show the magnitude and sign of the calculated pure shear strains. Superimposed on the contour diagrams are lines which locate the boundaries between zones of positive and negative shear strain. Because these boundaries locate zones along which the sign of the shear strain changes, they are also the loci of points of zero shear strain and should therefore be bordered by contour lines with an appropriate range of values. The numerical data from which the contour diagrams were plotted, however, suggested that the width of the transition zone between adjacent regions of positive and negative shear strains was narrow - of the order of millimeters. Further, the magnitude of the shear strains developed either side of the transition zones can be seen in the contour diagrams to be similar, irrespective of the sense of the shear rotation. For these reasons it was considered appropriate to present the shear strain data with the contours crossing the boundaries of zones of opposite sign. It should be noted, however, that the boundary lines locate a narrow transition zone with high shear strain gradients.

Contour intervals given in the strain diagrams vary between diagrams. Intervals were selected mainly in order to provide sufficiently detailed data to illustrate the nature of complex strain patterns.

One of the principal assumptions in the method used to estimate soil strains around the model pile (Appendix D) is that displacements vary linearly along a boundary between the nodes of an element, and therefore that strain varies linearly within the elements. Whilst this assumption is usually acceptable if elements located in zones of high displacement are small, or if the relative node displacements are small, it is not generally acceptable for use in the case of soils undergoing significant remoulding. As illustrated in Figure A.9 (Appendix A), the sand grain displacements around the model pile vary approximately logarithmically with distance from the pile axis. The assumption of linear variation of displacements along element boundaries is therefo . inherently incorrect.

The technique of averaging the calculated strains at nodes common to a number of deformed elements, assists in reducing errors due to the assumption of linear strain variation within an element. Accordingly, it is suggested in view of the finely graded mesh pattern adopted, that the strain contour diagrams shown in Figures 6.8 to 6.19 and 6.21 to 6.44 provide a reasonable indication of both the magnitude and pattern of strains applicable to the various soil movements around the model pile. (See Appendix A4.) In the soil boundary layer lying against the pile surface where displacement gradients are high, limitations in the sand movement measurement equipment and data manipulation techniques indicate that this region is likely to contain the least accurate data.

It will be noticed that in the majority of the strain diagrams, strain contours are plotted beyond the perimeter of the plotted displacement fields. This is another consequence of the assumption of linear variation of displacement between element nodes. It is also a consequence of dividing the soil continuum into elements of prescribed dimensions with nodes that do not necessarily bear a relationship to natural boundaries such as the "zero" displacement contours. Where the "zero" displacement contours transect an inter-nodal boundary, it was necessarily assumed in applying the finite element approximation that this contour was located at the outermost node, and strains were calculated accordingly. However, because the zero displacement contours are more correctly the loci of displacements at the limits of measurement accuracy corresponding to 15 to 20 plotter units of displacement, the transference of "zero" displacements to the outermost node of an element provides partial compensation for the non-zero nature of the "zero" displacement contour.

In addition to the specific data given in the strain diagrams, various other strain related parameters may be derived either by calculation, or approximately, by superposing the diagrams. Values of Poissons ratio in the radial plane may be obtained from the ratio of the minor principal strains and the corresponding major principal strains. Poissons ratios applicable to circumferential strains may be obtained from the ratio of circumferential strains and major principal strains. The radial and circumferential Poissons ratios do not have the same values throughout the strain fields.

This data has not been presented as there is sufficient other data available to estimate these parameters.

The rectangular grids used to estimate soil strains during both pile installation and static load testing are shown in Figures 6.7 and 6.20 respectively. The grid in Figure 6.20 is essentially similar to that of

Figure 6.7, extended upwards to include a portion of the pile shaft by increasing the number of elements.

6.4.2 Symmetry in the Strain Diagrams

One of the boundaries of the finite element grid used to estimate soil strains was located along the pile axis (the axis of symmetry of the displacement field) below the point of he pile shoe. Because there were no elements with equal magnitude, but opposite in direction displacement data located across this boundary, the calculated strain data at times violates the requirements of symmetry on this axis.

For symmetry, principal strain directions at nodes lying on the axis should be parallel to the axis, and the axis should also be a locus of a zero shear strain contour. The strain diagrams have, however, been presented using the calculated data. Where necessary, the major principal strain directions and maximum shear strain data given on this axis should be re-interpreted as required by symmetry.

In the case of the shear strain diagrams, this procedure will satisfy sign convention, but the magnitude of the strain contours on either side of the axis will be the same and the contours themselves will be duplicated across the axis. (See also 6.4.1, discussion on shear strain contours bounding loci of zero shear strains.)

6.4.3 Strains during Pile Installation

The soil strains estimated for the three increments of pile penetration monitored during pile installation are given in Figures 6.8 to 6.19. It is appropriate to compare the strain patterns of similar strain diagrams relevant to each penetration increment.

Major principal strains, shown in Figures 6.8 and 6.14 were, except for a small area opposite the shoe collar in Figure 6.14, all compressive. Below the level of the shoe collar, the strain contours generally lie approximately parallel to the face of the shoe cone leading to a wedge shaped distribution of strain contours around the pile toe, which in 3-dimensions would appear as a series of concentric cones. Peak strains occur in both diagrams at both the point, and base, of the shoe cone. The diagrams are consistent with one another as regards major features, though Figure 6.14 contains a zone of tensile strains opposite the shoe collar. This zone is reflected in Figure 6.19 as a zone of dilative volumetric strain. The approximately parallel nature of the strain contours suggests that the magnitude of the major principal strains was heavily influenced by the geometry of the pile shoe.

Minor principal strain contours, referring to the minor principal strains calculated for the biaxial strain state applicable to a radial plane, are given in Figures 6.10 and 6.16.

These diagrams show that, apart from two small areas opposite the shoe collar in Figure 6.10 and adjacent to the grout column in Figure 6.16, the minor principal strains were associated with extension. This is to be expected due to the Poisson effect. Where the minor principal strains were compressive, the relevant volumetric strains (Figures 6.13 and 6.19) indicate areas of volume decrease. As with the major principal strain diagrams, the minor principal strain contours are approximately parallel to the face of the shoe cone below the level of the shoe collar, but differ near the pile axis by becoming roughly horizontal. Peak strains occur at the point of the pile shoe and at the base of the shoe cone in Figure 6.16.

In the area located between one and two pile diameters opposite the base of the shoe cone, the magnitude of the minor principal strains exceeds the magnitude of the major principal strains indicating a Poissons ratio of greater than unity.

Figures 6.11 and 6.17 show the circumferential strain patterns induced in the soil during pile installation.

Both figures show similar features with simple concentric contours indicating extension which peak in magnitude at the pile toe. Near the shoe collar, the circumferential strains indicate that compression occurred in the circumferential direction above the base of the shoe cone. Over most of the displacement field, circumferential strains are intermediate in magnitude between the major and minor principal strains, and therefore correspond to the intermediate principal strain. Close to the pile shoe, however, the circumferential strains are algebraically smaller than the strains referred to as the minor principal strains. In such regions, the circumferential strains also become the minor principal strains. The diagrams are consistent with the pattern of circumferential strains which may be expected from bulk outward movement of the soil away from the pile shoe.

The diagrams showing major principal strain directions are given in Figures 6.9 and 6.15. These directions are equivalent to the resultants of the X and Y displacement components at the nodes of the finite element grid and record the trajectories of the node displacements as well as the major principal strain directions. The two diagrams are essentially similar, though the directions at individual nodes vary, and show that the flow pattern of the soil around the pile toe was similar for both displacement increments. It is clearly shown in the diagrams that the directions change from nearly vertically downwards below the pile shoe, through horizontal, to upwards above the shoe collar. Near the base of the shoe cone, considerable major principal strain direction rotations occurred. In this region, the plotted directions roughly follow a logarithmic spiral. As noted in Section 6.2.1, the displaced soil encroached onto the grout column during pile penetration. Confirmation of this observation is obtained in these two figures from the strain directions given at the nodes lying against the grout column above the shoe collar.

Although not obvious in Figures 6.9 and 6.15, the calculated major principal strain directions at nodes located on the pile axis below the point of the pile shoe, were oriented at small angles in the range 0 to 4 degrees to the pile axis. For symmetry, the major principal strain directions on this axis should be parallel to the axis along the pile axis, and in view of the comments given in 6.4.2, it should be assumed that they are parallel.

Contour diagrams showing maximum shear strains are given in Figures 6.12 and 6.18. Both these figures can be divided into three distinct strain fields separated by two zero shear strain contours. The largest field comprises clockwise shear strains and occupies a zone located below an inclined zero shear strain contour extending outwards and downwards from the base of the shoe cone. Within this zone, in Figure 6.18, two patches of counter-clockwise shear strains occur close to the pile axis near the point of the pile shoe. Figure 6.12 shows no indication of similar features, and it is not known whether they are significant.

Above this zone lies an area of counter-clockwise shear strains with peak shear strains occurring near the base of the shoe cone towards which both zero shear strain contours converge. The third shear strain field comprising clockwise element rotations is located between the edge of the pile and a zero shear strain contour extending upwards in an S shape from near the base of the shoe cone. Following the comments of 6.4.2, a zero shear strain contour should be assumed along the pile axis.

This shear strain pattern is consistent with the indications of the major principal strain direction diagrams.

Volumetric strains have been plotted in Figures 6.13 and 6.19. In both diagrams, complex strain patterns are developed close to the pile shoe, and there are some major differences in the patterns in an area located about one pile diameter from the pile axis at the level of the base of the shoe cone. Elsewhere the diagrams are similar. A broad perimeter zone comprising compressive volumetric strains encloses the entire strain field. Enclosed within this field is a zone of dilatant volumetric strains which is developed below the level of the base of the shoe collar and extends to the face of the shoe cone. Offset from the face of the shoe cone, but partially enclosed within this dilatant zone, is a tongue of compressive strain contours which meet the shoe cone about three quarters of the way up from the point of the shoe. Although dimensions and details differ, above the base of the shoe cone similar patches of dilatant and compressive volumetric strains can be identified.

6.4.4 Soil Strains during Static Loading

Soil stains estimated from the sand grain displacement diagrams recording soil movements observed during static load testing of the model pile are given in Figures 6.21 to 6.44. As before, the strain behaviour observed in similar strain diagrams relevant to each penetration increment are compared.

Major principal strains are shown in Figures 6.21, 6.27, 6.33 and 6.39. Except for two small zones in Figure 6.21, the diagrams indicate that the major principal strains were compressive. The magnitude of the strains were highest in a small zone immediately below the point of the pile shoe. Above this, relatively smaller strains were calculated near the point of the shoe, but they increased upwards along the face of the shoe towards the base of the cone. In all the diagrams, additional zones of high strain magnitude occurred below the pile toe and close to the pile axis. Adjacent to the pile shaft, the initially simple pattern of essentially sub-parallel strain contours seen in Figure 6.21 becomes complex in subsequent diagrams as a result of the irregular shape of the pile shaft previously referred to in 6.2.2c. As with the sand grain displacement diagrams, the strain contours converge in the region of the shoe collar.

The minor principal strain diagrams (Figures 6.23, 6.29, 6.35 and 6.41) are generally inconsistent and contain a number of considerably different features particular to each diagram. Most of the estimated minor principal strains were negative however, indicating extension, but zones of compressive strain do occur. One of the largest of these is adjacent to the pile shaft in Figure 6.29.

Except for Figure 6.24, the circumferential strain diagrams show very similar strain patterns which closely resemble those produced from the dynamic installation soil displacement data. Figure 6.24 contains zones of compressive circumferential strain in the perimeter of the displacement field. It is not certain that this data is meaningful. The contour pattern in the strain diagrams suggests bulk movement of the soil away from the pile throughout the displacement field.

The diagrams showing the major principal strain directions (Figures 6.22, 6.28, 6.34 and 6.40) are generally consistent with one another, though directions vary considerably in the area opposite the pile shaft located at between 2 and 3 pile diameters from the pile axis. Most of the calculated strain directions are downwards and/or outwards from the pile axis, but in the area of variable directions, some upward movements are indicated. Along the axis of symmetry below the point of the pile shoe the major principal strain directions should be assumed to be parallel to the axis.

Four strain fields can be identified in the shear strain diagrams given in Figures 6.25, 6.31, 6.37 and 6.43. These include a wedge of counter-clockwise shears adjacent to the pile axis below the point of the pile shoe, a large zone of clockwise shear adjacent to the inclined force of the shoe, a second wedge shaped zone of counter-clockwise shear separated from, but opposite, the shoe collar, and a zone of clockwise shear extending outwards from the pile shaft, but continuous downwards into the other zone of clockwise shear strains. The diagrams show progressive features with the magnitude of the shear strains increasing with the penetration of the pile. As in other strain diagrams, the strong influence of the shape of the pile shaft above the shoe on the strain pattern is noticeable.

Significant differences can be detected between the shear strain diagrams prepared from data obtained during pile installation, and those prepared from the static load testing data. In particular, the static load test diagrams contain an additional zone of counter-clockwise shear strain below the point of the pile shoe and the zone of clockwise shear adjacent to the pile shaft is continuous into that adjacent to the face of the shoe cone.

The volumetric strain patterns shown in Figures 6.26, 6.32, 6.33 and 6.44 differ somewhat from one another in detail, but as with the equivalent pile installation diagrams, contain three fields of similar features below the shoe collar. A broad zone of compressive strains occupies the perimeter of the displacement field. The greatest volumetric compressions in this field occur close to the axis of symmetry about one pile diameter below the point of the pile shoe. Enclosed within this and extending to the face of the shoe cone is a field of dilatant strains, while close to the shoe, there are patches of compressive strains which do not persist between diagrams. Occupying a narrow boundary layer against the pile shaft is a zone of volume increases. Beyond this boundary layer the volumetric strains are mainly compressive. About 70 mm above the top of the shoe collar where the "waist" in the pile shaft occurs, compressive volumetric strains are developed against the pile shaft. Above the shoe collar, the volumetric strain magnitude against the pile shaft in Figures 6.38 and 6.44 is the same, suggesting constant volume shear on this interface.

6.4.5 Summary

1 The distribution and magnitude of various components of strain calculated from the sand grain displacement data obtained during both pile installation and subsequent static loading have been presented in the form of contour diagrams. The strains were calculated using a finite element solids of revolution method presented by Clough (1965).

2 The patterns of strain at different increments of pile penetration have been described and compared.

3 Strain patterns obtained from impact installation data differ from those obtained from static loading data, indicating different mechanisms of soil failure.

4 Volumetric strains are generally complex, but show that pile penetration is accompanied by both dilatation and compression in the soil below the pile shoe. In particular, a zone of dilatation occurs close to the pile shoe and compression occurs in a perimeter zone.

5 Contour lines locating zero volumetric strains do not necessarily conform to the loci of shear strains. This indicates that shear at constant volume did not occur in a manner which could be simply correlated to the magnitude of the shear strain.

6 Dilatation was observed against the pile shaft during static load testing as a result of shear on this interface. The volumetric strain data against the pile shaft in Figures 6.32 and 6.37 suggest that constant volume shear occurred against the pile shaft during the "drained" load test. This may be expected as shear with no volume change is known to be associated with high shear strains. The "drained" load test was carried out after the "submerged" load test during which the pile had already been loaded to failure and displaced approximately 5mm (see Figure 5.6, pg 5.15)."

7. INTERPRETATION OF MODEL TEST RESULTS

7.1 Introduction

The results of detailed measurements on the movement of sand particles around a model MV pile during installation and loading in sand under laboratory conditions, have been presented in the preceding two chapters. Contour diagrams have been used to illustrate the magnitude of the accumulated soil displacements given in terms of horizontal and vertical components of movement during a sequence of penetration increments. These data have been converted into various components of strain, the results of which have also been presented in the form of contour diagram of strain magnitude. All the soil displacement measurements were made near the pile toe over a narrow toe movement range at an embedment ratio (L/d) of about 12,5.

Loads on the pile shaft and toe were also researched during the tests. All loads relating to the interaction between the pile and the soil, however, are estimates based on an approximate correction to the measured loads for friction between the pile and the glass panel of the sandbox. Whilst the suggested pile/soil loads are therefore not necessarily accurate, it is considered that they are reasonably representative of the correct loads.

Based on this experimental data, some preliminary observations can be made on the bearing capacity characteristics of the model MV pile. In the following discussion, the design proposals given by Jelinek (1962) have not been compared with the model pile test results. Jelinek's work was largely empirically based and was mostly intended for MV piles under tension loading, whereas the model pile test refers to compression loading. It is worth noting, however, that Jelinek's work supported the concept of a critical depth of embedment (see Section 7.2), and that limiting skin friction capacities of the order of 180 kPa to 220 kPa were determined in sandy deposits. At depths less than the critical depth given as 10m for typical piles, friction capacities of between 90 (L/d = 10) and 220 kPa were recorded.

7.2 Shaft Friction

The average friction capacity, fs, of a pile shaft in sand is generally expressed by a Mohr-Coulomb equation using effective stress parameters of the form:

$$fs = qv. Ks. \tan\delta \qquad (7\text{-}1)$$

where qv is the overburden pressure at a given depth, Ks is a lateral earth pressure coefficient and δ is the friction angle between the pile and the soil. It is known, however, that the friction stress on straight shaft preformed driven piles in an homogenous sand does not necessarily increase linearly with depth as predicted by this equation (Meyerhof [1976], Vesic [1963, 1964, 1970], Robinsky and Morrison [1964], O'Neill [1983], Hanna and Tan [1973], Mansur et al [1956]). Explanations for this phenomen are generally ascribed to the development of "arching" in the soil around the shaft (Vesic 1963, 1965) preventing full lateral transference of stress from the overburden onto the pile shaft. Mansur et al (1956, p.461) also note that "Compressive forces at the pile tip result in a zone of radial shear beneath the pile tip, which causes a radial movement of the soil that will tend to reduce the lateral earth pressure and skin friction of the sand on the surface of the pile immediately above the tip". Tomlinson (1977) observes that when a pile is driven into a sand, whip in the pile shaft and continuous shearing in the soil at the pile interface, leads to the formation of a shell of loose sand against the shaft with a shell of more dense sand beyond this.

Various skin friction distribution patterns have been noted in the literature. These range from linearly increasing with overburden pressure until a limiting skin friction stress, $f\ell$, is reached after which the stress remains constant (Meyerhof, [1976], Vesic, [1977], through irregular distributions (Robinsky and Morrison, 1964), to triangular or parabolic. The "critical depth", Dc, at which $f\ell$ is reached, ranges from L/d = 10 to L/d = 30 for loose and dense sands respectively. Vesic (1970) performed a series of instrumented tests on 457mm diameter closed ended steel pipe piles driven to various depths in dense and medium dense sands. The skin friction distribution for the piles tested at L/d ratios of 13 and 20 were nearly symmetrically parabolic. Vesic (1977, p.19) suggests that the limiting friction stress is, "for a given sand deposit, a function of the initial sand density and probably over-consolidation ratio of the deposit only". He notes though that $f\ell$ for tapered piles of similar dimensions to a straight pile, may be nearly twice that of the straight pile. Meyerhof (1976) goes further and notes that skin friction, as well as being a function of Ks, δ and L/d, is also dependent on the method of pile installation, compressibility of the soil, Ko - the initial horizontal earth pressure coefficient, and on pile size and shape. He concludes that "reliable values of Ks and $f\ell$ can only be deduced from load tests on piles at the given site".

There is a considerable range in the published values of Ks and δ in equation (7-1) (Bowles [1982] and Tomlinson [1977] review some of the published information). It appears that while the theoretical basis of equation (7-1) is sound, considerable care is needed in selecting suitable values of Ks and δ, particularly in view of Meyerhof's observations noted above (cf Tomlinson's [1977] comments Section 2.4).

Skin friction data for the model MV pile given in Tables 6.5 and 6.6 (Pg 6.38) corrected for friction with the glass front panel have been analysed in terms of equation (7-1). The components of the various terms in this equation are listed in Tables 7.1 and 7.2 (Pg 7.6). In these tables, it has been assumed following the discussion in Appendix E.4 that the friction angle, δ, is 40° and has the same value along the full length of the shaft.

The calculated values of Ks in Tables 7.1 and 7.2, particularly over the upper portions of the pile shaft, exceed published values for piles by significant amounts. They are, however, of a similar order of magnitude to the passive earth pressure coefficients given by Bowles (1982, p.382) for "relatively large" retaining wall movements against the backfill. The theoretical passive lateral earth pressure coefficient, Kp, can be calculated from the expression, (where ϕ= friction angle)

$$Kp = (1 + \sin \phi)/(1 - \sin \phi)$$

For a friction angle of 40°, which it has been suggested is applicable to the soil against the pile shaft, Kp is obtained as Kp = 4,6. Attempts to impose a lateral earth pressure in excess of that permitted by a Kp coefficient obtained by the above calculation, results in yield in the soil. It is suggested that the calculated Ks values in Table 7.1 were therefore obtained using incorrect data.

TABLE 7.1: Friction stress soil parameters determined by equation (7-1). Load test in submerged sand (for L4 load increment)

Submerged unit weight = 6,73 kN/m^3
δ average = 40°
tan δ = 0,84

Position	Depth m	qv kN/m2	Shear Stress fs kN/m2	Ks = $\frac{fs}{qv.\tan\delta}$
SG4/SG3	0,120	0,808	13	19,2
SG3/SG2	0,328	2.207	38	20,5
SG2/SG1	0,536	[illegible]607	24	7,9
SG1/Toe	0,695	4,677	6	1,5
Mid-shaft	0,365	2,456	23,31(av)	11,3(av)

TABLE 7.2: Friction stress soil parameters determined by equation (7-1). Load test in drained sand (for L8 load increment)

Unit weight = 17,49 kN/m^3
δ average = 40°
tan δ = 0,84

Position	Depth m	qv kN/m2	Shear Stress fs kN/m2	Ks = $\frac{fs}{qv.\tan\delta}$
SG4/SG3	0,120	2,099	19	10,8
SG3/SG2	0,328	5,737	44	9,1
SG2/SG1	0,536	9,375	29	3,7
SG1/Toe	0,695	12,156	14	1,4
Mid-shaft	0,365	6,384	23,8(av)	5,6(av)

TABLE 7.3: Friction stress soil parameters from equation (7-1) related to grout pressure. Load test in submerged sand (for L4 load increment)

Submerged unit weight (grout) = 11 kN/m^3

δ average = 40°

tan δ = 0,84

Position	Depth m	qv kN/m3	Shear Stress fs kN/m2	Ks = fs / qv.tan δ
SG4/SG3	0,220	2,420	13	6,4
SG3/SG2	0,428	4,708	38	9,6
SG2/SG1	0,636	6,995	24	4,1
SG1/Toe	0,795	8,745	6	0,8
Mid-shaft	0,365	4,015	23,3 (av)	6,9 (av)

The fluid grout which eventually cures to form the shaft of an MV pile is usually more dense than the surrounding soil. This was the case with the model tests. It is reasonable to suggest therefore that a more correct lateral earth pressure coefficient could be related to the hydrostatic pressure of the grout column before it cured. It will be recalled that for the model tests the grout column was approximately 100mm longer than the pile shaft because of the use of a grout reservoir at the top of the pile. Table 7.3 provides a revised version of Table 7.1 on the basis that qv was related to the grout pressure inside the pile shaft before the grout cured. (It is suggested that a similar exercise is not applicable to the drained test due to stress relief during removal of the water) (see Section 6.3.5).

It will be noted that Ks in Tables 7.2 and 7.3 are of a similar order of magnitude, though still, except for Ks near the pile toe (SG1/Toe), higher than published values for piles. Even if the corrected shear stress data listed in Tables 6.5 and 6.6 (from which Tables 7.2 and 7.3 were derived) were over-estimated by a factor of 2, the calculated Ks values are still somewhat higher than normally accepted. An explanation for this may lie in the way the MV pile is manufactured (though some of the difference is probably also due to error in the assumed friction angle δ).

If the friction block analogy for the forces on the pile toe as described in Appendix E.2 is accepted, then the possible magnitude of the horizontal stress developed at the pile toe during pile installation can be estimated. In Appendix E.2 an equation (E-1) is developed which expresses the load Fvt applied to the pile shoe as the sum of various components,

$$Fvt = Fvh + Fvs + Fvv + Fvn \qquad \text{(E-1)}$$

Expressions for these components each contain a term q which is defined as the resultant stress acting on the shoe surface at an angle of 40° to the vertical during pile installation and at 30° to the vertical during static loading. As discussed in Appendix E.3 a further correction of about 55 N should be applied to equation E-1 to allow for friction between the plastic separator strip (attached to the shoe), and the glass front panel.

If it is assumed that the toe load of 1138N, measured during the immediate post-installation static load test was representative of the soil resistance excluding any dynamic influences, then Fvt = 1138 - 55N, or Fvt = 1083 N. On substituting the values of the various parameters suggested in Appendix E.2 into equation (E-1), the resultant stress qu, acting at 40° from the vertical is determined as 308 kPa. The horizontal component of this stress is 198 kPa. According to Meyerhof (1976), toe resistance, like shaft resistance, also varies linearly with depth down to a critical depth. Consequently the horizontal stress developed at the pile toe may also vary approximately linearly with depth. Toe resistance during the post-installation test was measured at a toe depth of about 790mm, the centre of pressure on the conical shoe being at about 750mm. The overburden stress corresponding to this embedment was, under the submerged conditions, about 5 kPa. The ratio of the horizontal to vertical stress corresponding to a form of lateral earth pressure coefficient at failure of the soil around the pile toe, was thus about 40. Figures and 5.4 (rear pocket) showing the horizontal displacement components of the sand grains, indicate that at the bottom of the shoe collar, soil movements towards the pile axis were recorded. This movement is likely to have provided some stress relief to the highly compressed soil during pile penetration, possibly reducing Ks to the order of magnitude shown in Table 7.3, and to a level compatible with the hydrostatic pressure in the grout column. It would appear then that due to the method of construction, MV piles are able to beneficially exploit the remoulding of the sand around the pile toe in the following ways:

(a) The fluid grout column following the pile shoe does not disturb the soil at the shaft interface.

(b) High lateral earth pressures developed during toe penetration are at least partially preserved against the pile shaft.

(c) On curing, the fluid grout bonds with the surrounding sand forming a rough interface, probably with a friction angle greater than that of the undisturbed soil.

The relatively low shaft friction capacity measured near the pile toe may be due to a combination of both arching, and a process related to the previously noted explanation by Mansur et al (1956). It is considered that the slight "neck" observed in the pile shaft near

SG1 is unlikely to have had any major influence on the average shaft capacity over the lower pile shaft. It has been noted in 6.2.2(b) that sand grain displacement contours for the static load tests tend to converge in the region of the shoe collar. This is particularly clear in the vertical displacement diagrams, for example, Figure 5.15 (rear pocket). Opposite the shoe collar, a large area of upward movements was also recorded. The shear strain data derived from Figure 5.15 and given in Figure 6.37 shows the presence of a wedge of generally low magnitude positive shear strains opposite the shoe collar. Volumetric strains within this wedge shaped zone (Figure 6.38) are likewise generally of low magnitude. The sum of these features suggests that this wedge shaped zone represents a relatively undisturbed area which opposes downward displacement of the soil, thereby reducing the volume of soil subjected to shear originating at the shaft interface. Whilst the effect of this zone is one of arching, it appears to be a consequence of the soil displaced by the pile shoe.

The soil displacement data presented does not extend high enough above the pile shoe to indicate the depth over which this zone is active, but it may extend as far up the pile shaft as SG2. Mansur et al (1956, p.461) note that in their tests the "... skin friction appears to be reduced significantly for a distance of from 6 ft to 12 ft above the pile tip". For the pipe pile diameter tested by Mansur et al (op.cit.) this corresponds to a length of between 3 and 8 pile diameters above the pile shoe. SG2 for the laboratory test reported here was located about 5 pile diameters above the pile shoe and thus lies within the skin friction reduction zone reported by Mansur et al. If it is accepted that soil movements around the pile toe were similar in both Mansur's tests and the present test, the shaft load at both SG1 and SG2 may well have been influenced by upward soil displacements due to toe penetration.

7.3 Toe Resistance During Static Loading

The toe capacity of driven piles in sand has traditionally been estimated using conventional bearing capacity formulae as described in 2.1. Equation (2-3) shows the general form of such formulae. For piles in sands, the general formula can be simplified. The term referring to soil cohesion can be eliminated and, since the term containing N_γ is relatively small compared to the Nq term, the N_γ term can be neglected. Further, the shape factors for circular and square piles are generally similar. Hence, the simplified expression for piles in sand becomes:

$$Qb = Ab\ (pv.Nq) \qquad (7\text{-}3)$$

or in terms of stress

$$qb = pv.Nq \qquad (7\text{-}4)$$

Pile toe capacity is thus simply a function of overburden pressure and a coefficient, Nq. It is known, however, that pile toe resistance does not increase without bound with depth, and in an homogenous sand deposit, reaches a limiting value at a critical depth related to the density of the soil (Meyerhof, 1976).

The "bearing capacity factor", Nq, is a dimensionless number which incorporates a theoretical model describing yield in the soil surrounding the pile toe.

Various theoretical models have been proposed. These generally assume a perfectly elastic - perfectly plastic stress-strain behaviour for the soil and obtain slip-line field solutions which satisfy limiting equilbrium equations and stated boundary conditions in terms of stresses. Coyle and Castello (1981, p.977) show how Nq varies with soil friction angle, Ø, for eleven different theoretical versions of yield around a pile toe. Although a direct comparison of the eleven different versions of Nq is not valid due to the different conditions for which the formulae were developed, the range in published Nq values indicates a need for considerable caution in adopting a particular value. Another cause for concern when using published Nq values, is the extreme sensitivity of Nq to the angle of internal friction of the soil. As Coyle and Castello (op. cit., p.967) note: "It is evident that there are major deviations from one theory to another, leading to the conclusion that the true failure mechanism is not generally well understood." They also note (p.967) that none of the theories "... considers the side resistance of the soil along the pile shaft, or a possible inter-dependence between side and point resistances." Some of the deviations from the major theoretical assumptions applied in deriving an Nq value for a given soil, compared to the findings of the model pile test data, are noted below.

7.3.1 Limiting Equilibrium Models and Model Test Observations

In most derivations of Nq, the soil around the pile toe is assumed to remain homogenous and unchanged by pile installation. This is a reasonable assumption in the case of bored piles, but is clearly unacceptable for driven piles. Meyerhof (1959) investigated the effect of densification around the pile toe and derived revised values of Nq to account for it. The volumetric strain diagrams (given in the rear pocket), show that for the model pile at least, the soil around the pile toe was cleary not homogenous and was subjected to a complex strain history.

Generally the shape and position of the failure surface is assumed to follow a mathematically defined pattern.

Vesic (1965) presents diagrams which show the forms of various slip-line field proposals which are mostly based on some form and portion of a logarithmic spiral. Whilst the theoretical sliding surface need not agree with the sliding surface observed in the soil (due to the assumptions for soil behaviour) the model pile test results indicate notable differences to the theoretical models.

A possible slip-line field around the model pile is shown in Figure 7.1. This diagram was drawn using the principal strain direction data of Figure 6.34 and superimposing theoretical conjugate shear planes inclined at an angle of $45 - \phi/2$ to the major principal strain axis. The angle ϕ, was selected as 40° on the basis of triaxial test results (Figures 7.2, 7.3) and following the comments given in Appendix E. Because the density of the soil varies around the pile, ϕ will also vary, but it is considered that this will not affect the major features of Figure 7.1. Also shown in Figure 7.1 are the boundaries (simplified and smoothed) between zones of positive and negative shear strain which were taken from Figure 6.37 (rear pocket).

In contrast with the theoretical limiting equilibrium models of yield around a pile toe, no bounding slip-line between plastically and elastically deformed zones is detectable in Figure 7.1. Also, no passive "Rankine

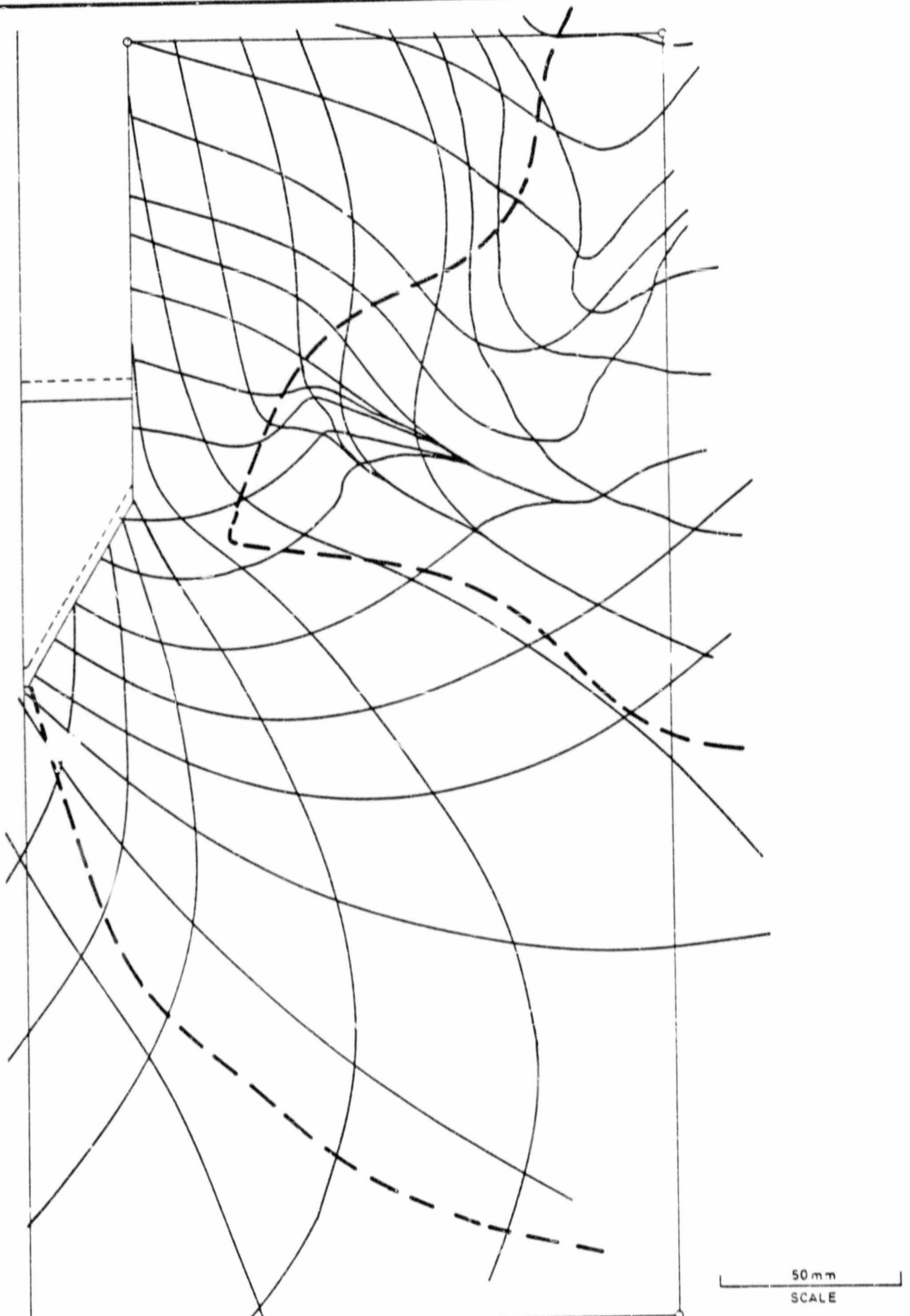

FIGURE 7.1 : A possible slip-line field around the model pile

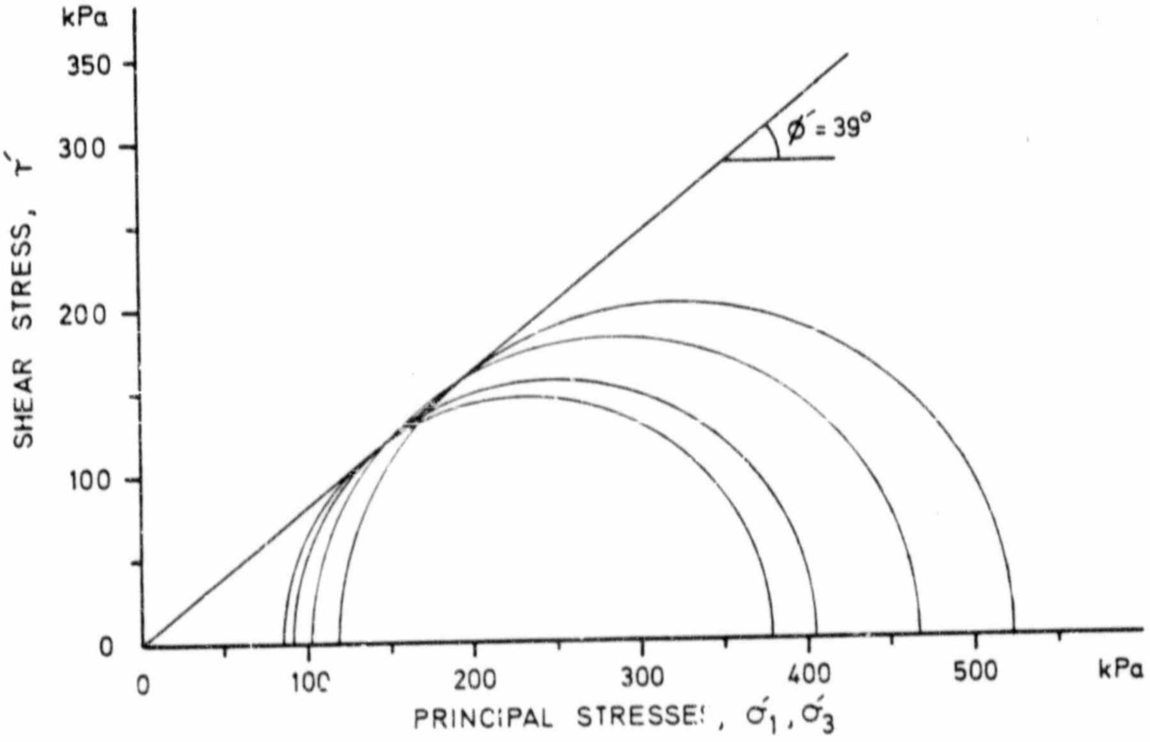

FIGURE 7.2a

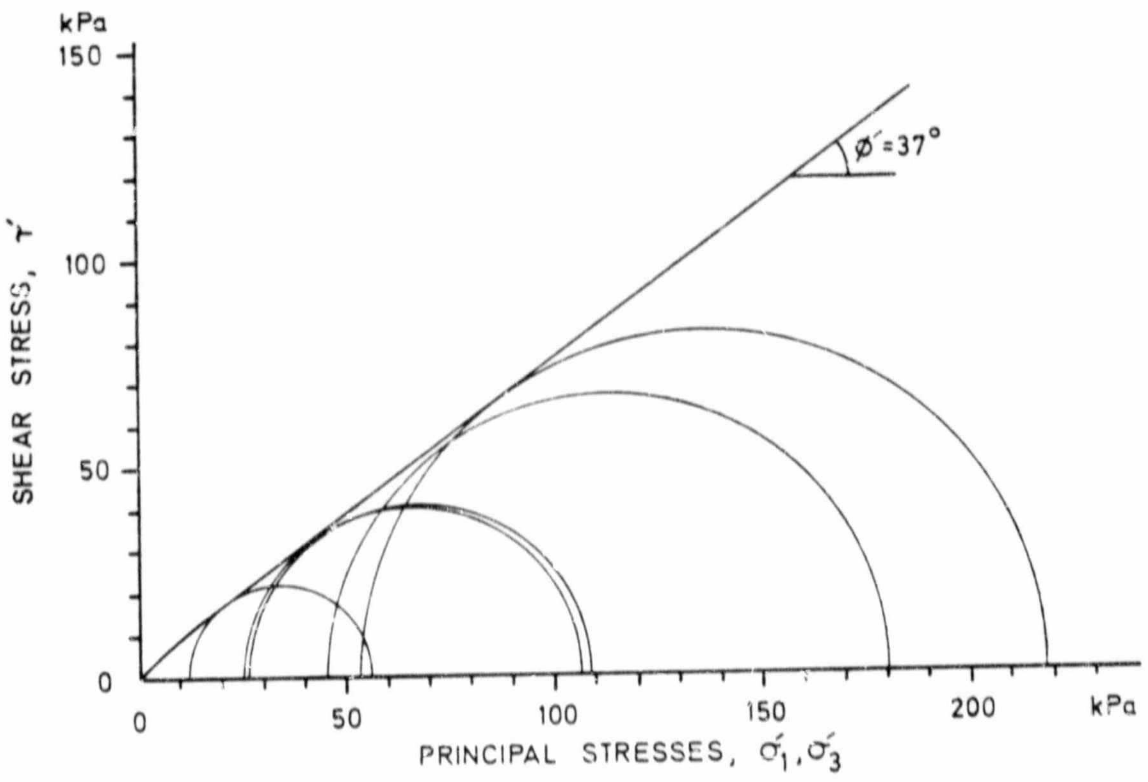

FIGURE 7.2b

FIGURE 7.2 : Test sand shear strength data from triaxial tests

wedge" bordering the shear zone adjacent to the pile shoe is detectable. Instead, the shear pattern in Figure 7.1 most closely resembles one proposed by Skempton et al (1953), based on a model for expansion of a cavity in an elastic solid. Also, within the wedge shaped zone of positive shear strains opposite the shoe collar, slip-lines originating at the pile toe and at the pile shaft converge and coalesce developing a complex and irregular shear pattern. This pattern appears to indicate interference between two regular slip-line fields; the one associated with shaft friction, and the other with toe movements. The slip-line pattern given in Figure 7.1 also suggests that nowhere is the surface of the pile parallel to the slip-lines drawn for the soil. This in turn implies that slip along the pile surface does not occur on a plane of maximum stress obliquity. In view of reservations expressed in Appendix A.4 and Appendix D regarding the accuracy of the sand grain displacement data in zones of high displacement gradients, this observation may be premature.

In view of the proposed slip-line field pattern given in Figure 7.1, it is suggested that use of conventional bearing capacity formulae for determination of toe capacity is, at least in the case of the model pile, inappropriate. Further, interdependence between point and side resistances would appear to have been demonstrated. Because of the similarity of the model pile failure pattern to that proposed by Skempton et al (1953), their predicted Nq has been compared to the Nq factor indicated by the model test. A comparison has also been obtained for Coyle and Castello's empirical design values. These findings are discussed in 7.3.2.

7.3.2 Bearing Capacity Factory, Nq, for the Model Pile

It is unlikely that an Nq bearing capacity factor obtained from a laboratory scale model pile test is applicable to full-scale pile tests. Some comment on this has been given in 4.1. Estimated scaling factors become more uncertain when, as has been shown is 7.3.1, the premises on which the scale factors are based may be in error. The following comments can therefore provide only a preliminary guide as to the possible range of Nq values suitable for MV piles.

It was recorded in Sections 6.3.1 and 6.3.2 that the model pile toe capacities for the three different static load tests were:

(a) 677 kPa Immediate post-installation test (fluid grout)

(b) 604 kPa Submerged sand test (cured grout)

(c) 791 kPa Drained sand test (cured grout)